Model for Nonlinear Electric Field Control in End-Winding Region of an Electrical Machine

Egorov Dmitry, Lindh Pia, Pyrhönen Juha

DOI: 10.1109/ICEM51905.2022.9910906

Model for Nonlinear Electric Field Control in End-Winding Region of an Electrical Machine

D. Egorov, P. Lindh, J. Pyrhönen

***Abstract* – The electric potential at the surface of a stress grading system (SGS) of an electrical machine is estimated analytically by means of a new one-dimensional model approach. The analytical tool is presented for electric field grading materials (FGMs) having power-law field-dependent conductivity, field independent conductivity, and field independent permittivity terms as dielectric parameters. The model-calculated data are compared with finite element results for SGS with 15 distinct FGM options that are used in SGSs of medium voltage motors or generators. The results indicate that the analytical tool is suitable for the basic analysis of electric field in an electrical machine end-winding region both during sinus and pulse voltage conditions.**

***Index Terms*--Rotating electrical machines, converter fed motors, end windings, nonlinear field control, stress grading, stress grading system, electric field distribution**

I. Introduction

In medium-voltage rotating electrical machines, stress-grading systems (SGSs) are utilized for winding insulation surface smooth electric potential transition from machine's stator stack earth potential to phase voltage [1]. Machine geometry and the levels of the applied voltages may easily result in local electric field stresses at the surface of the main insulation. Electric field strength exceeding the air ionization threshold is a prerequisite for partial discharge (PD) activity. Local PDs cause increased chemical and thermal stresses that facilitate insulation system failure in an electrical machine [2].

Fig. 1 depicts a conventional structure of an SGS. Conducting armor tape (CAT) mitigates PDs inside machine's stator slot via equalizing insulation surface potential. Stress grading tape (SGT) is used to avoid local electric field enhancements due to different electric potentials of the phase electrode and CAT. Materials with field dependent electric conductivity ($\sigma(E) \sim E^n$) are used for SGTs to design efficient SGSs under spatial and thermal constraints in machine's end winding region [3], [4].

The theoretical performance of an SGS is mostly studied by finite element analysis (FEA) [1], [2], [4], [5]. Computational efforts increase significantly when taking the nonlinearity of the applied SGT material into account in the modelling. FEA-based analysis of SGS under pure sine supply may be well simulated in frequency domain [5]. Nevertheless, analyzing an SGS under pulse conditions requires time-domain studies because of the strong nonlinearities in the dielectric properties of SGT materials. Therefore, a simple tool for preliminary analysis is of interest. The model results may be used as a relevant starting point for detailed FEA, if required.

Several researchers have studied analytically the profile of electric field along the surface of SGS in a machine's end winding region. Studies [6]-[8] provide similar solutions for field grading materials (FGM) having field independent dielectric parameters. The results of [6]-[8] may be used in the analysis of electric potential along CAT, which is usually manufactured with field independent dielectric parameters. An analytical solution for materials having extremely high nonlinearity is discussed in [9], [10]. These materials are not suitable for practical SGTs because of their thermal limitations, although they provide the most homogenous electric field distribution along an SGT. Finally, the analytical considerations for the material having power-law field dependent conductivity ($\sigma(E) \sim E^n$) are proposed in [11]. The accuracy of the introduced analytical considerations in [11] was limited in some cases because field independent conductivity and permittivity components were omitted in the formulation. In practice, these components are present in practical materials having nonlinear field-dependent conductivity [3].

This paper complements the theoretical findings presented in [11]. The potential distribution in an end winding region is derived for FGMs with power-law ($\sigma(E) \sim E^n$) field

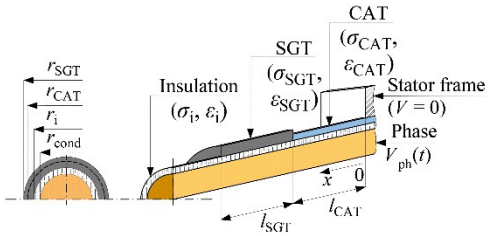

Fig. 1. Sketch of a typical SGS in the end winding region of an electrical machine, which operates at a medium voltage. Radially symmetrical coordinate system is used for the analytical modeling purposes. The main insulation with radius r_i, conductivity σ_i, and relative permittivity ε_i covers the phase electrode with radius r_{cond}. CAT with radius r_{CAT}, conductivity σ_{CAT}, and relative permittivity ε_{CAT} is provided along the main insulation inside machine's stator slot region. CAT ends at distance l_{CAT} from the stator slot exit. SGT having conductivity σ_{SGT}, radius r_{SGT}, and relative permittivity ε_{SGT} starts from CAT's end and reaches to the distance l_{SGT} along the main insulation' surface. Time-dependent electric potential $V_{ph}(t)$ is applied to the phase electrode. Stator frame has zero electric potential.

D. Egorov is with the Department of Electrical Engineering, Lappeenranta-Lahti University of Technology, FI-53851 Finland (e-mail: dmitry.egorov@lut.fi).

P. Lindh is with the Department of Electrical Engineering, Lappeenranta-Lahti University of Technology, FI-53851 Finland (e-mail: pia.lindh@lut.fi).

J. Pyrhönen is with the Department of Electrical Engineering, Lappeenranta-Lahti University of Technology, FI-53851 Finland (e-mail: juha.pyrhonen@lut.fi).

dependent conductivity, field independent conductivity, and field independent permittivity as dielectric properties. The paper is organized as follows. The analytical formulation for the problem is presented in Section 2. The model-calculated data are compared with FEA results for 15 distinct SGT materials in Section 3. The results are analyzed in Section 4 and Section 5 concludes the paper.

II. 1-Dimensional Modelling Approach For End-Winding Region

Conventionally used analytical approach assumes SGS as a thin layer with much higher conductivity than the conductivity of the main insulation. Thus, the electric field strength along SGS is almost purely tangential and the insulation system in machine' end winding region can be represented via the equivalent circuit that is depicted in Fig. 2 [6]-[10].

In Fig. 2, $I_D(x, t)$ and $I_L(x, t)$ are displacement and leakage terms of the current in the main insulation per unit length, respectively. These can be estimated with the electric potential $V_I(x, t)$ along insulation thickness:

$$I_D(x,t)+I_L(x,t)=C_I\frac{\partial V_I(x,t)}{\partial t}+S_I\frac{V_I(x,t)}{r_i-r_{cond}}, \quad (1)$$

where C_I and S_I are capacitance and conductance of the main insulation per unit length:

$$C_I=\frac{2\pi\cdot\varepsilon_0\cdot\varepsilon_i}{\ln\left(r_i/r_{cond}\right)}, \quad (2)$$

$$S_I=\frac{2\pi\cdot\sigma_i\cdot\left(r_i-r_{cond}\right)\cdot\left(r_i/r_{cond}\right)}{\ln\left(r_i/r_{cond}\right)}. \quad (3)$$

The current along (x-axis) FGM (CAT or SGT) $I_{FGM}(x, t)$ may be written with $V_I(x, t)$:

$$I_{FGM}(x,t)=\left(S_{FGM}\cdot\frac{\partial V_I(x,t)}{\partial x}+\frac{\partial}{\partial t}\left(C_{FGM}\cdot\frac{\partial V_I(x,t)}{\partial x}\right)\right), \quad (4)$$

where capacitance C_{FGM} and conductivity S_{FGM} of the FGM per unit length are defined as:

$$C_{FGM}=\pi\cdot\varepsilon_0\cdot\varepsilon_{FGM}\cdot\left(r_{FGM}^2-r_i^2\right), \quad (5)$$

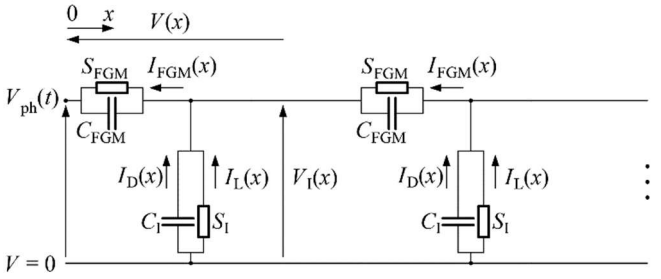

Fig. 2. Description of a machine's insulation system at the end winding region based on 1-dimensional modelling approach. In the equivalent circuit, the phase electrode is grounded and the phase voltage $V_{ph}(t)$ is applied to the stator stack. In such a case, the proposed theoretical findings have a solution in real numbers. The boundary conditions may be summarized as follows: 1) $V_I|_{(x=0,\,t)}=V_{ph}(t)$; 2) $V_I|_{(x=\infty,\,t)}=0$; 3) $\partial V_I/\partial x|_{(x=\infty,\,t)}=0$. Other analytical investigations on the topic [6]-[9] indicate that the chosen boundary conditions are relevant for the study of practical SGSs in electrical machines. The electric potential along the FGM' surface $V(x)$ is defined with $V_I(x)$ and $V_{ph}(t)$, i.e. $V(x)=V_{ph}(t)-V_I(x)$.

$$S_{FGM}=\pi\cdot\sigma_{FGM}\cdot\left(r_{FGM}^2-r_i^2\right), \quad (6)$$

and r_{FGM} is radius, σ_{FGM} is conductivity, and ε_{FGM} is relative permittivity of the considered FGM (see Fig. 1). Inserting (1), (4) into Kirchhoff's current conservation law $I_L(x, t) + I_D(x, t) = \partial I_{FGM}(x, t) / \partial x$ leads to partial differential equation:

$$S_I\frac{V_I(x,t)}{r_i-r_{cond}}+C_I\frac{\partial V_I(x,t)}{\partial t}=\frac{\partial}{\partial x}\left(S_{FGM}\cdot\frac{\partial V_I(x,t)}{\partial x}+\frac{\partial}{\partial t}\left(C_{FGM}\cdot\frac{\partial V_I(x,t)}{\partial x}\right)\right), \quad (7)$$

which will be analyzed further.

A. Previous progress on the topic

This subsection describes previous relevant findings in analytical estimation of electric potential along SGSs. FGMs for CAT are usually manufactured with conductivity σ and relative permittivity ε that do not exhibit considerable changes under the magnitude of applied electric field E, i.e. $\sigma_{CAT}(E) = \sigma_{CAT}$ and $\varepsilon_{CAT}(E) = \varepsilon_0\varepsilon_{CAT}$. The solution of (7) with parameters of CAT, boundary conditions in Fig. 2, and rewriting $V_I(x, t) = V_I(x) \times \xi(t)$ is of the form:

$$V_I(x,t)=V_{ph}(t)e^{-x/\sqrt{k_{ind}(t)}}, \quad (8)$$

where

$$k_{ind}(t)=\frac{\pi\cdot\left(r_{CAT}^2-r_i^2\right)\cdot\left(\sigma_0\cdot\xi(t)+\varepsilon_0\varepsilon_{CAT}\left(\partial\xi(t)/\partial t\right)\right)}{S_I\cdot\xi(t)/\left(r_i-r_{cond}\right)+C_I\times\left(\partial\xi(t)/\partial t\right)}. \quad (9)$$

The solution for AC voltage supply having electrical frequency f can be derived in the frequency domain, i.e. $\xi(t)=e^{j2\pi ft}$. In this study, the solution under pulse supply with the pulse rise time τ_p is studied only for the time $0 \le t \le \tau_p$ with $\xi(t) = t / \tau_p$. Similar to (8) solutions are presented for FGMs with electric field independent dielectric properties in [6]-[9].

Applicable FGMs used to manufacture SGT demonstrate a strong increase in conductivity with the increase of applied electric field strength. The study reported in [11] provides an analytical solution for the FMGs with power-law field dependent conductivity $\sigma_{SGT}(E) = \sigma_0 \times (|E / E_0|)^\alpha$, where σ_0 is conductivity at low field strength, E_0 is a threshold field strength, and α is the exponential nonlinearity coefficient. The field independent conductivity and permittivity dielectric components are ignored in [11]. The solution of (7) in this case assuming $\partial V_I(x) / \partial t \ge 0$ and boundary conditions in Fig. 2 is available for $0 \le V_I(x) \le V_{ph}$:

$$x+C=\sqrt[\alpha+2]{2}\,\frac{(\alpha+2)V_I(x)}{\alpha}\left(\frac{(\alpha+2)\left(V_I\right)^2}{k_{res}(t)(\alpha+1)}\right)^{-\frac{1}{\alpha+2}}, \quad (10)$$

where

$$k_{res}(t)=\frac{\pi\cdot\left(r_{SGT}^2-r_i^2\right)\cdot\sigma_0\cdot\left(\xi(t)\right)^{\alpha+1}}{\left(S_I\cdot\xi(t)/\left(r_i-r_{cond}\right)+C_I\times\left(\partial\xi(t)/\partial t\right)\right)\cdot E_0^{\alpha}}. \quad (11)$$

The constant C in (10) may be estimated with (8) when knowing the length of CAT l_{CAT} and the electric potential V_I on the insulation surface at the end of CAT.

The study reported in [11] demonstrates that (10) is useful to estimate some important parameters of SGSs both under sine and pulse voltage conditions. Nevertheless, omitting field independent conductivity and permittivity components in the formulation of (10) may result in incorrect model results in some operational modes of SGS. These cases are characterized with a considerable share of the electric current in terms that are caused by the field independent dielectric properties of practical SGT materials [11]. This matter is tackled in the following subsection.

B. Field control with practical field grading material used in stress grading tapes

The relative permittivity ε_{SGT} in practical SGTs is assumed field independent, i.e. $\varepsilon_{SGT}(E) = \varepsilon_0\varepsilon_{SGT}$. The conductivity comprises both field independent and field dependent terms. This study uses a typical formulation of SGT conductivity of the form:

$$\sigma_{SGT}(E) = \sigma_0 \times \left(1 + \left|E/E_0\right|^{\alpha}\right). \quad (12)$$

Setting parameters of the SGT in (7) and rewriting $V_I(x, t) = V_I(x) \times \xi(t)$, (7) transforms to:

$$V_I(x)\left(S_I \cdot \xi(t)/\left(r_i - r_{cond}\right) + C_I \frac{\partial \xi(t)}{\partial t}\right) =$$

$$\frac{\partial}{\partial x}\left(\frac{\partial V_I(x)}{\partial x} \cdot \pi \cdot \left(r_{SGT}^2 - r_i^2\right) \cdot \left(\begin{array}{l}\left(\sigma_0 \cdot \xi(t) + \varepsilon_0 \varepsilon_{SGT} \frac{\partial \xi(t)}{\partial t}\right) \\ + \frac{\sigma_0 \cdot \left|\xi(t)\right|^{\alpha} \cdot \xi(t)}{\left|E_0\right|^{\alpha}} \cdot \left|\frac{\partial V_I(x)}{\partial x}\right|^{\alpha}\end{array}\right)\right). \quad (13)$$

The solution of (13) is available in the analytical form for the case $\partial V_I(x) / \partial t \geq 0$, which is suitable for estimation of many practical parameters of SGS. Thus, (13) turns to:

$$V_I(x) =$$

$$\frac{\left(\pi \cdot \left(r_{SGT}^2 - r_i^2\right) \times \left(\sigma_0 \cdot \xi(t) + \varepsilon_0 \varepsilon_{SGT} \frac{\partial \xi(t)}{\partial t}\right)\right)}{S_I \frac{\xi(t)}{r_i - r_{cond}} + C_I \times \left(\partial \xi(t) / \partial t\right)} \cdot \frac{\partial}{\partial x}\left(\frac{\partial V_I(x)}{\partial x}\right) +$$

$$\frac{\pi \cdot \left(r_{SGT}^2 - r_i^2\right) \cdot \sigma_0 \cdot \xi(t)^{\alpha+1}}{E_0^{\alpha}\left(S_I \frac{\xi(t)}{r_i - r_{cond}} + C_I \times \left(\partial \xi(t) / \partial t\right)\right)} \cdot \frac{\partial}{\partial x}\left(\left(\frac{\partial V_I(x)}{\partial x}\right)^{\alpha+1}\right). \quad (14)$$

Applying boundary conditions from Fig. 2 and rewriting $V_I(x, t) = V_I(x) \times \xi(t)$, the solution of (14) for $0 \leq V_I(x) \leq V_{ph}$ is of the form:

$$x + C = \frac{(\alpha+2)\left(a_1(t) z^2 + a_2(t) z^{\alpha+2}\right)}{\alpha z \sqrt{a_1(t) z^2 + a_2(t) z^{\alpha+2}}} -$$

$$\frac{2\sqrt{a_1(t) a_2(t)}\sqrt{\frac{a_1(t)}{a_2(t) z^{\alpha}} + 1} \cdot z^{\frac{\alpha+4}{2}} \cdot \sinh^{-1}\left(\frac{\sqrt{a_1(t)} \cdot z^{\frac{\alpha}{2}}}{\sqrt{a_2(t)}}\right)}{\alpha z \sqrt{a_1(t) z^2 + a_2(t) z^{\alpha+2}}}, \quad (15)$$

$$V_I(x) = \sqrt{a_1(t) z^2 + a_2(t) z^{\alpha+2}}$$

where

$$a_1(t) = \frac{\pi \cdot \left(r_{SGT}^2 - r_i^2\right) \cdot \left(\sigma_0 \cdot \xi(t) + \varepsilon_0 \varepsilon_{SGT} \left(\partial \xi(t) / \partial t\right)\right)}{S_I \cdot \xi(t) / \left(r_i - r_{cond}\right) + C_I \cdot \left(\partial \xi(t) / \partial t\right)}, \quad (16)$$

$$a_2(t) = \frac{2\pi \cdot (\alpha+1) \cdot \left(r_{SGT}^2 - r_i^2\right) \cdot \sigma_0 \cdot \xi(t)^{\alpha+1}}{(\alpha+2) \cdot \left(S_I \cdot \xi(t) / \left(r_i - r_{cond}\right) + C_I \times \left(\partial \xi(t) / \partial t\right)\right) \cdot E_0^{\alpha}}, \quad (17)$$

The constant C in (15) is estimated with (8) similarly as it was discussed in case of (10). Equations (9), (16), and (11), (17) are similar to each other. This is an indication that power-law field dependent conductivity, field independent conductivity, and field independent permittivity dielectric parameters of the material are included in the newly introduced (15). Although (15) requires some calculations of $V_I(x)$ with respect to z, it is rather easy to handle with the basic tools that are available in most commercial computational environments. The presented analytical considerations are verified further.

III. Comparison Of FEA- and Model- Calculated Results

FEA-based software is found to be an effective tool for the detailed analysis of practical SGSs [1]-[5]. In this chapter, the model-calculated data is compared with results provided by 2D COMSOL® Multiphysics using its AC/DC add-on. The parameters of the SGS are reproduced from [12] and are depicted in Fig. 3 and Table I. The publication-survey-based measured data on the nonlinear SGTs for electric motors and generators are summarized in Table II, as it was discussed in [11]. The data is reproduced at the temperatures close to 80 ºC. The dielectric properties of the materials may change due to the Joule loss generated in SGS. According to the Authors best knowledge, an accurate equation-based thermal model has not been presented for SGSs. The thermal effects are not considered in this study.

The basic analysis of an SGS concentrates on estimation of maximum electric field strength E_{max} on the surface of the SGS and along the length of the SGS in the axial direction of the machine. In a correctly designed SGS E_{max} occurs at the beginning of SGT region, i.e. approximately at the distance l_{CAT} from the stator slot exit. Insufficient length of SGT may not provide a smooth enough potential transition from the phase electrode to the potential of CAT, thus, the local electric field enhancement may occur at the end of SGS. The proposed (15) is not capable to simulate the charge accumulation phenomenon that occurs at the surface of SGT at electrical potential values close to the V_{ph} [11]. In this

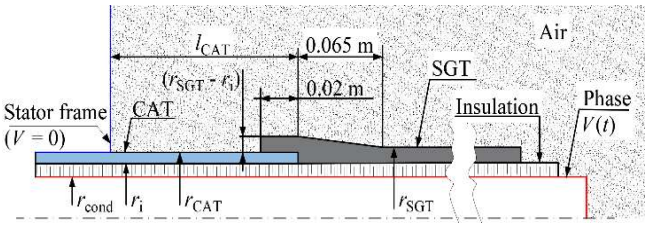

Fig. 3. Sketch of SGS used in the 2D FEA simulation. The data for the model are reproduced from [12].

study, the relevant geometrical length of SGT along machine's end winding region is evaluated with penetration length parameter Δ [9], which defines the distance from the beginning of an SGT region where the electric potential is reduced by fraction $(e-1)/e$:

TABLE I
INPUT DATA OF SGS USED IN THE ANALYSIS

Parameter	
Radius of the phase conductor r_{cond} [m]	0.01
Radius of the main insulation r_i [m]	0.0124
Radius of the CAT r_{CAT} [m]	0.0129
Radius of the SGT r_{SGT} [m]	0.0131
Length of the CAT l_{CAT} [m]	0.055
Insulation conductivity σ_i [S/m]	2.01×10^{-15}
CAT conductivity σ_{CAT} [S/m]	0.01
Air conductivity σ_{air} [S/m]	10^{-18}
Dielectric constant of the insulation ε_i	4
Dielectric constant of the air ε_{air}	1
Dielectric constant of the SGT ε_{SGT}	20
Dielectric constant of the CAT ε_{CAT}	20
Rise time of the pulse τ_p [s]	12×10^{-6}
Magnitude of the pulse V_{peak} [V]	11500
Frequency of the AC supply voltage f [Hz]	50
Phase voltage magnitude at AC supply $V_{ph,sin}$ [V]	7780

TABLE II
REPORTED PROPERTIES OF NONLINEAR FGMS USED IN SGSS OF MEDIUM VOLTAGE ROTATING ELECTRICAL MACHINES

FGM	σ_0 [S/m]	E_0 [kV/m]	α
FGM1	2.07×10^{-8}	120	3.24
FGM2	2.67×10^{-8}	100	4.16
FGM3	2.38×10^{-8}	100	3.43
FGM4	1×10^{-9}	90	3.8
FGM5	4.12×10^{-11}	150	5.1
FGM6	7.05×10^{-12}	200	4
FGM7	4.96×10^{-10}	200	8.16
FGM8	8.73×10^{-9}	100	3.66
FGM9	6.07×10^{-7}	130	3.76
FGM10	1.54×10^{-7}	70	2.40
FGM11	2.89×10^{-9}	140	10.60
FGM12	7.48×10^{-9}	225	6.50
FGM13	9.94×10^{-6}	250	3.84
FGM14	4.01×10^{-8}	125	3.65
FGM15	6.83×10^{-9}	100	3.17

$$\Delta = x\left(V_{ph} - \left(\frac{V_{ph} - V_1}{e}\right)\right) - x(V_1). \quad (18)$$

The comparison between the FEA- and analytically calculated values of the maximum electric field strength with respect to penetration length are depicted in Fig. 4a for purely sinusoidal supply. Fig. 4b provides FEA- and model calculated data for the case of pulse supply. The analytical considerations include estimation of electrical potential in a CAT region by means of (8).

The data in Fig. 4a and Fig. 4b are converted to Table III and Table IV, where η_1 and η_2 denote the relative error between results of (15) and FEA, and results of (10) and FEA, respectively.

The influence of SGT's permittivity on the distribution of the electric field is evaluated in SGS with FGM5 at pulse voltage supply. The data in Table I and Table II indicate that

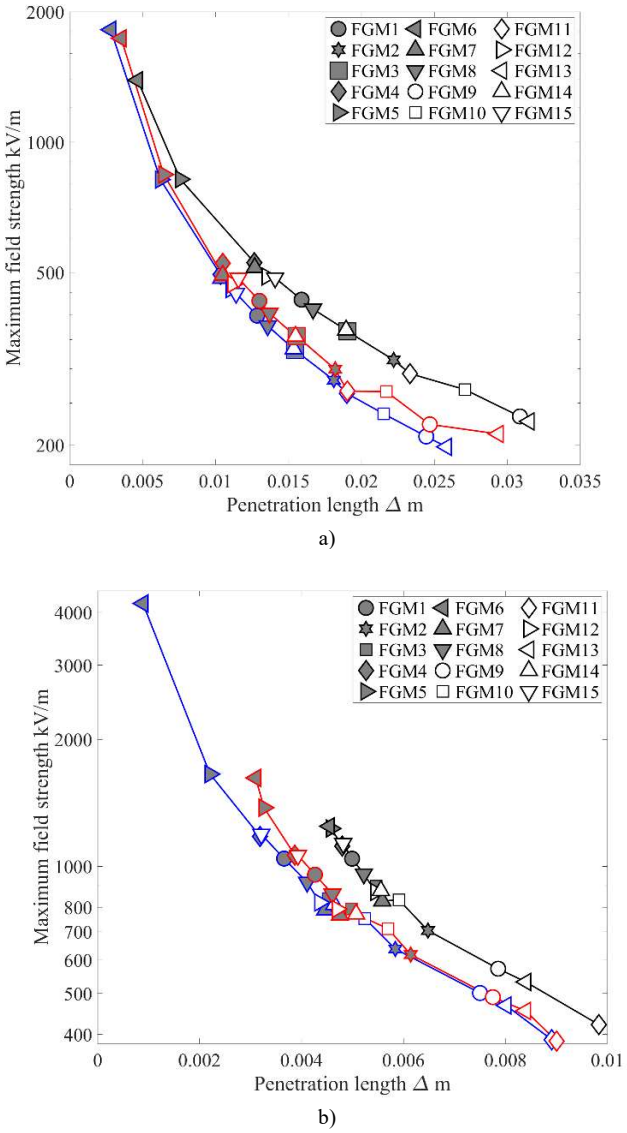

Fig. 4. Model- and FEA- calculated data on maximum electric field strength along SGT E_{max} with respect to penetration length Δ. a) at pure sine supply. The applied voltage is characterized with $V_{ph,sin} = 7780$ V and $f = 50$ Hz; b) at pulse supply. The applied voltage is characterized with $V_{peak} = 11500$ V and $\tau_p = 1.2 \times 10^{-5}$ s. The FEA-calculated results are depicted by the markers with black border lines. The calculated data with newly introduced (15) are depicted with the markers having red border lines. The markers with blue border lines depict the calculated data with (10), which ignores the field independent dielectric properties of SGT.

the potential distribution along the SGT made from FGM5 at pulse conditions will be mostly affected by nonlinear-resistive- and field-independent- capacitive- current density components while the effect of the field independent resistive current density will be marginal. The geometry and parameters of the SGS are the same as in Fig. 3 and Table I. The electrical conductivity of CAT is assumed to be high ($\sigma_{CAT} = 10^{10}$ S/m) to exclude inaccuracies related to the estimation of electric potential along CAT. In such a case, the electric potential transition from the stator stack to the potential of phase electrode of the machine occurs mostly along SGT. A pulse voltage with magnitude $V_{peak} = 11500$ V and distinct pulse rise times τ_p is applied to the SGS. A

comparison of the model- and FEA-calculated data is depicted in Fig. 5.

TABLE III
RELATIVE ERROR BETWEEN FEA AND ANALYTICAL RESULTS AT AC SUPPLY

FGM	$\eta_{1,\Delta}$ [%]	$\eta_{2,\Delta}$ [%]	$\eta_{1,E\max}$ [%]	$\eta_{2,E\max}$ [%]
FGM1	−18.22	−19.17	−0.61	−8.11
FGM2	−18.04	−18.47	−4.85	−10.18
FGM3	−18.22	−18.87	−2.55	−9.52
FGM4	−17.16	−18.41	−0.27	−6.13
FGM5	−14.92	−17.97	2.54	−0.210
FGM6	−24.32	−39.61	24.97	30.77
FGM7	−17.32	−18.08	−4	−5.57
FGM8	−17.88	−18.64	−2.14	−8.49
FGM9	−20.01	−20.81	−4.12	−10.09
FGM10	−19.89	−20.58	−1.08	−12.04
FGM11	−18.39	−18.57	−8.89	−9.97
FGM12	−17.34	−18.15	−3.98	−6.42
FGM13	−6.71	−17.99	−6.46	−12.64
FGM14	−18.28	−18.97	−3.25	−9.60
FGM15	−17.86	−19	−0.20	−7.83

TABLE IV
RELATIVE ERROR BETWEEN FEA AND ANALYTICAL RESULTS AT PULSE SUPPLY

FGM	$\eta_{1,\Delta}$ [%]	$\eta_{2,\Delta}$ [%]	$\eta_{1,E\max}$ [%]	$\eta_{2,E\max}$ [%]
FGM1	−14.57	−26.71	−8.33	0.06
FGM2	−5.21	−9.89	−12.29	−9.54
FGM3	−8.90	−17.22	−11.74	−6.60
FGM4	−19.36	−33.58	−4.810	5.42
FGM5	−28.78	−51.85	12.07	34.58
FGM6	−31.84	−80.44	30.20	237.28
FGM7	−14.89	−20.06	−7.42	−4.78
FGM8	−11.80	−21.30	−10.36	−4.41
FGM9	−1.32	−4.53	−14.38	−12.41
FGM10	−3.60	−11.32	−14.62	−9.64
FGM11	−8.39	−9.38	−8.57	−7.90
FGM12	−13.86	−20.14	−8.91	−5.58
FGM13	−0.07	−4.63	−14.61	−12.02
FGM14	−8.73	−16.43	−11.96	−7.32
FGM15	−18.41	−33.33	−6.24	5.14

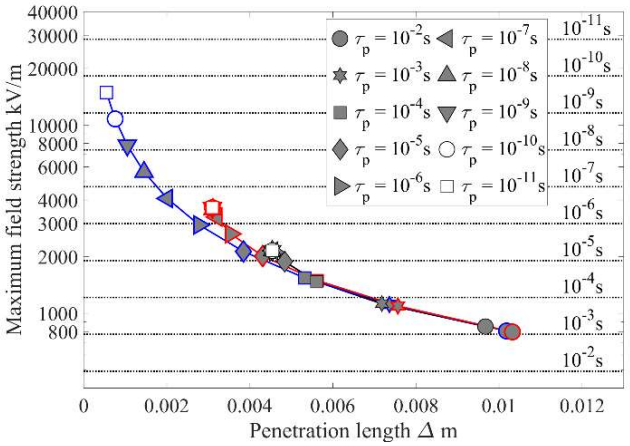

Fig. 5. Analytically- and FEA- calculated maximum electric field strength along SGT E_{max} with respect to penetration length Δ at pulse supply with different pulse rise times τ_p for SGS with SGT made from FGM5. The parameters of the system and depicted in Fig. 3 and Table I, except $\sigma_{CAT} = 10^{10}$ S/m and varying pulse rise time τ_p. The FEA-calculated results are depicted with the markers having black borders. The model calculated data with newly introduced (15) are depicted with the markers having red borders. The markers with blue border lines represent model calculated data obtained with (10), which ignores the field independent dielectric properties of SGT. The values of E_{SCLF} calculated with (20) for each τ_p are depicted with black dotted lines.

For comparative purposes, the calculated data on the space charge limited field E_{SCLF} are depicted in Fig. 5. Studies [13]-[15] refer to E_{SCLF} as the maximum field strength achieved in nonlinear dielectric with specific dielectric properties under applied voltage with angular frequency ω. The value of E_{SCLF} is estimated when the resistive and capacitive current density components in the material are equal, i.e. in the case the formulation of SGT' dielectric properties chosen is:

$$E_{SCLF} = \sqrt[\alpha]{\frac{\left(\left|\varepsilon_{SGT}\varepsilon_0\,\partial\xi(t)/\partial t\right| - \sigma_0\xi(t)\right)\cdot E_0^{\alpha}}{\sigma_0\cdot\left(\xi(t)\right)^{\alpha+1}}}. \qquad (19)$$

IV. DISCUSSION

Analytically calculated results for Δ and E_{max} in Fig. 4 are close to the FEA-results. The data in Table III for AC supply demonstrate overall better accuracy of the presented analytical considerations compared to (10) that ignores field independent dielectric properties of FGM. The value of E_{max} estimated with (15) demonstrates a slightly worse inaccuracy in comparison to (10) for SGT with FGM5. This is related to the space charge accumulation phenomenon in an actual SGS.

The penetration length estimated with newly introduced (15) is closer to the FEA-calculated data at pulse supply as it follows from Fig. 4b and Table IV. In contrary, the calculated values of maximum field strength E_{max} demonstrate slightly reduced accuracy in comparison to (10). The inaccuracy in the estimation of E_{max} is caused by combined effect of the inaccuracy of electric potential estimation along CAT region, local electric field enhancement due to the geometry of actual SGS, and space charge accumulation phenomenon on the boundary of main insulation and FGM.

The data in Table IV for FGM5 and FGM6 demonstrate significant improvement in the accuracy of the results calculated with (15) in comparison with (10). The observed difference in results is caused by field independent current density terms that are considered in the formulation of (15). The studied formulation on SGT dielectric properties estimates resistive current density component J_{res} and capacitive current density component J_{cap} as follows:

$$J_{res} = \sigma_0\cdot\left(1+\frac{E^{\alpha}\cdot\xi(t)}{E_0^{\alpha}}\right)\cdot E\cdot\xi(t), \qquad (20)$$

$$J_{cap} = \left|\varepsilon_0\cdot\varepsilon_{SGT}\cdot E\cdot\partial\xi(t)/\partial t\right|. \qquad (21)$$

Fig. 6 depicts the current density terms for FGM5 and FGM6 with respect to the magnitude of the applied electric field strength. The maximum field strength for FGM5 is 820 kV/m and 1228 kV/m at pure AC and pulse supply, respectively. The shares or capacitive and resistive current density terms are $J_{cap}/J_{res}|_{E=820\text{ kV/m}} \approx 0.23$ and $J_{cap}/J_{res}|_{E=1228\text{ kV/m}} \approx 7.86$, as it can be seen in Fig. 6. The results obtained with (10) for FGM5 at AC supply are still close to FEA-calculated data since the resistive current density terms prevail over capacitive current density. The pulse supply case for SGS with FGM5 results in dominating

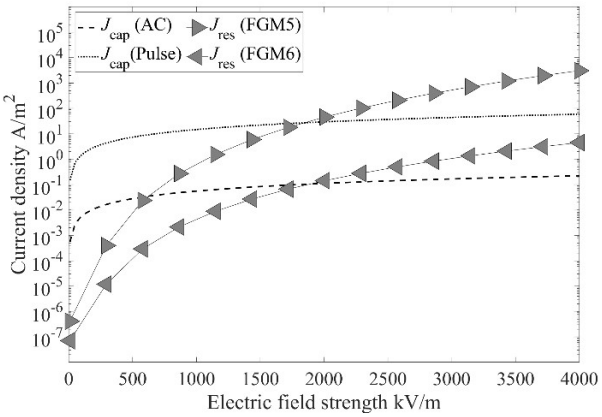

Fig. 6. Resistive and capacitive ($\varepsilon_{SGT} = 20$) current density terms for FGM5 and FGM6 at pure sine supply ($f = 50$ Hz, frequency domain) and at the pulse supply ($\tau_p = 1.2 \times 10^{-5}$ s, $t = \tau_p$).

capacitive current components, and, thus, inaccurate modelling results if only nonlinear resistive current density term is considered.

The FEA-calculated values of E_{max} for FGM6 are 1390 kV/m and 1244 kV/m at AC supply and pulse supply, respectively. The data in Fig. 6 for FGM6 indicates that $J_{cap} / J_{res}|_{E = 1390\ kV/m} \approx 3.4$ and $J_{cap} / J_{res}|_{E = 1244\ kV/m} \approx 1397$. The calculated relations indicate that the capacitive current term cannot be ignored in study case with FGM6, and the analysis of SGT with (10) becomes irrelevant. The overestimated E_{max} with (15) for FGM6 might be related to space charge accumulation phenomenon that is neglected in the considered modelling approach.

The data in Fig. 5 demonstrate the importance of capacitive current density term in FGM. The maximum electric field strength E_{max} calculated with (10) demonstrates more accurate results in comparison with conventionally used concept of E_{SCLM}. Nevertheless, the analysis of (10) and (19) indicates that at infinitesimally small pulse rise time τ_p the maximum electric field in SGT E_{max} will attain infinity. This is controversial to the FEA-calculated data in Fig. 5 where the maximum field strength in SGT is approaching some value of limiting field. Consideration of (15)-(17) at pulse supply with infinitesimally small pulse rise time (i.e. $\partial\xi(t)/\partial t \rightarrow \infty$) results in the following maximum E_{max} in SGT:

$$E_{max} = V_1 \sqrt{\frac{2\varepsilon_i}{\left(\varepsilon_{SGT} \cdot \left(r_{SGT}^2 - r_i^2\right) \cdot \ln\left(r_i / r_{cond}\right)\right)}}. \quad (22)$$

The estimated $E_{max} = 3711$ kV/m with (22) in the case studied is illustrated in Figure 5. The analytically calculated E_{max} demonstrates a notable difference with the FEA results that estimate $E_{max} = 2150$ kV/m, as it follows from Fig. 5. The possible reason is the charge accumulation phenomenon that cannot be considered within the presented analytical approach. Nevertheless, the presented (22) demonstrates more accurate results in comparison to the previously used concept of E_{SCLF} and analytically calculated results with (10). The observed inaccuracy in model-calculated results in Fig. 5 occurs at the values of E_{max} where no practical SGSs operate due to the possible severe PD activity at the SGS surface.

V. Conclusions

The electric potential distribution along the surface of the SGS in machine's end winding region is analyzed with a newly introduced model. Theoretical findings are derived for FGMs having field independent conductivity, power-law field dependent conductivity, and field independent permittivity as dielectric parameters. The model- and FEA-calculated data for an actual SGS are compared for 15 nonlinear FGMs, which were considered in SGSs of the medium voltage rotating electrical machine. The model-estimated results demonstrate a sufficient match with FEA for maximum field strength along FGM surface E_{max} and the penetration length Δ. These parameters should be considered during design process of an effective insulation system in a medium voltage rotating electrical machine.

The introduced model demonstrates considerable accuracy improvement in situations where the current density due to the field independent dielectric properties of an FGM cannot be ignored. In such cases, the theoretical formulation based on nonlinear resistivity of FGM only may provide highly erroneous results. The previous considerations of maximum electric field strength in SGT (see (19) and (10)), in principle, enable infinite value of E_{max} if the pulse rise time is small enough. The newly introduced model converts to (22) that demonstrates the finite nature of E_{max}. Similar conclusion follows from FEA-calculated values of E_{max} depicted in Fig. 5.

Fig. 5 demonstrates that the new model shows a better agreement with FEA in comparison to (10) at the pulse supply. The results provided by the introduced model may still be inaccurate in case where the charge accumulation phenomenon cannot be ignored. The data in Fig. 4 and Fig. 5 indicate that a considerable difference between model and FEA estimated results occurs at regions where no practical SGS operates due to the possible severe PD activity.

VI. Appendix

Derivation process of (15)-(17) is provided in this Appendix. Setting $v = V_I(x)$, $p(v) = v' = \partial V_I(x) / \partial x$, and $v'' = p(v)\, \partial p(v) / \partial v$ (14) converts to:

$$v = a_1(t) \cdot v'' + a_2(t)\left(\left(\alpha + 2\right)/2\right) \cdot \left(v'\right)^{\alpha} \cdot v''. \quad (23)$$

Applying separation of variables technique and finding an indefinite integral convert (23) to:

$$V_I(x) = \sqrt{a_1(t) \cdot \left(\frac{\partial V_I(x)}{\partial x}\right)^2 + a_2(t) \cdot \left(\frac{\partial V_I(x)}{\partial x}\right)^{\alpha+2} - 2C_1}. \quad (24)$$

At the end of SGS the boundary conditions $V_I|_{(x = \infty,\ t)} = 0$ and $\partial V_I / \partial x\ |_{(x = \infty,\ t)} = 0$ (see Fig. 2), i.e. $C_1 = 0$. Setting $z = \partial V_I(x) / \partial x$ and $\partial / \partial x = \partial\partial z / \partial x \partial z$ (24) turns to:

$$V_I(x) = \sqrt{a_1(t) \cdot z^2 + a_2(t) \cdot z^{\alpha+2}}, \quad (25)$$

and

$$z = \frac{\partial z}{\partial x}\frac{\partial}{\partial z}\left(\sqrt{a_1(t)\cdot z^2 + a_2(t)\cdot z^{\alpha+2}}\right). \quad (26)$$

After several transformations (26) turns to:

$$x + C_2 = \frac{(\alpha+2)\left(a_1(t)z^2 + a_2(t)z^{\alpha+2}\right)}{\alpha z\sqrt{a_1(t)z^2 + a_2(t)z^{\alpha+2}}} - \frac{2\sqrt{a_1(t)a_2(t)}\sqrt{\frac{a_1(t)}{a_2(t)z^{\alpha}}+1}\cdot z^{\frac{\alpha+4}{2}}\cdot \sinh^{-1}\left(\frac{\sqrt{a_1(t)}\cdot z^{-\frac{\alpha}{2}}}{\sqrt{a_2(t)}}\right)}{\alpha z\sqrt{a_1(t)z^2 + a_2(t)z^{\alpha+2}}}. \quad (27)$$

The constant C_2 is subject to boundary conditions as it is discussed in Subsection 2.2 of the manuscript.

VII. REFERENCES

[1] A. Naeini, E. Cherney and S. Jayaram, "Temperature and electric field distributions along a form wound coil of an inverter-fed rotating machine with micro-varistor stress grading system," *IEEE Trans. Dielectr. Electr. Insul.*, vol. 27, no. 1, pp. 112-120, Feb. 2020.

[2] C. Staubach, T. Hildinger and A. Staubach, "Comprehensive electrical and thermal analysis of the stress grading system of a large hydro generator," *IEEE Electr. Insul. Mag.*, vol. 34, no. 1, pp. 37-49, Jan.-Feb. 2018.

[3] T. Christen, L. Donzel and F. Greuter, "Nonlinear resistive electric field grading part 1: Theory and simulation," *IEEE Electr. Insul. Mag.*, vol. 26, no. 6, pp. 47-59, Nov.-Dec. 2010.

[4] T. Umemoto *et al*, "Optimization of double-layer stress grading system for high voltage rotating electrical machines by electric field and thermal coupled analysis," *IEEE Trans. Dielectr. Electr. Insul.*, vol. 27, no. 3, pp. 971-979, Jun. 2020.

[5] C. Staubach, J. Wulff and F. Jenau, "Particle swarm based simplex optimization implemented in a nonlinear, multiple-coupled finite-element-model for stress grading in generator end windings," *2012 13th International Conference on Optimization of Electrical and Electronic Equipment (OPTIM)*, 2012, 2012.

[6] J. Rivenc, P. Bidan and T. Lebey, "Stress grading materials: a discussion on lumped elements circuits validity," *ICSD'98. Proceedings of the 1998 IEEE 6th International Conference on Conduction and Breakdown in Solid Dielectrics (Cat. No.98CH36132)*, Vasteras, 1998.

[7] J. Rivenc and T. Lebey, "An overview of electrical properties for stress grading optimization," *IEEE Trans. Dielectr. Electr. Insul.*, vol. 6, no. 3, pp. 309-218, Jun. 1999.

[8] L. Egiziano *et al*, "Electrical properties of different composite materials for stress relief in HV cable accessories," *Proceedings of 1995 Conference on Electrical Insulation and Dielectric Phenomena*, 1995.

[9] J. Rhyner and M. Bou-Diab, "One-dimensional model for nonlinear stress control in cable terminations," *IEEE Trans. Dielectr. Electr. Insul.*, vol. 4, no. 6, pp. 785-791, Dec. 1997.

[10] V. Tucci and J. Rhyner, "Comment on "1-dimensional model for nonlinear stress control in cable terminations"," *IEEE Trans. Dielectr. Electr. Insul.*, vol. 6, no. 2, pp. 267-270, Apr. 1999.

[11] D. Egorov and J. Pyrhönen, "One-dimensional model for the nonlinear resistive electric field control in medium-voltage rotating electrical machines," *IEEE Trans. Dielectr. Electr. Insul.*, vol. 28, no. 2, pp. 697-703, April 2021.

[12] N. N. Nam, "Non-linear Analysis of Electrical and Thermal Stress Grading System in Multi-Level Inverter-Driven Medium Voltage Motors," Shibaura institute of technology, Tokyo, 2014.

[13] S. Boggs, A. Kumada and T. Yoshimitsu, "Analytical approximations for the rotating machine end-turn field distribution," *IEEE Trans. Dielectr. Electr. Insul.*, vol. 22, no. 6, pp. 3146-3152, Dec. 2015.

[14] X. Qi, Z. Zheng and S. Boggs, "Engineering with nonlinear dielectrics," *IEEE Electr. Insul. Mag.*, vol. 20, no. 6, pp. 27-34, Nov.-Dec. 2004.

[15] S. Boggs, "Very high field phenomena in dielectrics," *IEEE Trans. Dielectr. Electr. Insul.*, vol. 12, no. 5, pp. 929-938, Oct. 2005.

VIII. BIOGRAPHIES

D. Egorov received the B.Sc. degree from the Moscow Power Engineering Institute, Moscow, Russia, in 2013, and the M.Sc. degree and D. Sc. (Tech.) degree in electrical engineering from the Lappeenranta-Lahti University of Technology (LUT), Lappeenranta, Finland, in 2015 and 2019, respectively. His research mainly concerns electrical machines and drives, in particular, the applications with the permanent magnets and development of new carbon-based materials for electrical machines.

P. Lindh (M'04, SM'17) born in Helsinki in 1969, received her M.Sc. degree in energy technology in 1998 and her D.Sc. degree in electrical engineering (Technology) in 2004 from Lappeenranta University of Technology (LUT), Lappeenranta, Finland. She is currently serving as an associate professor at the Department of Electrical Engineering in LUT Energy, Lappeenranta, where she is engaged in teaching and research of electric motors and electric drives.

J. Pyrhönen (M'06-SM'17) born in 1957 in Kuusankoski, Finland, received the Doctor of Science (D.Sc.) degree from Lappeenranta University of Technology (LUT), Finland in 1991. He became Professor of Electrical Machines and Drives in 1997 at LUT. He is engaged in research and development of electric motors and power-electronic-controlled drives. Prof. Pyrhönen has wide experience in the research and development of special electric drives for distributed power production, traction drives and high-speed applications. Permanent magnet materials and applying them in machines have an important role in his research. Currently, he is also researching new carbon-based materials for electrical machines.